One-pot microwave synthesized high-performance $BiVO_4/InVO_4$ heterojunction for photocatalytic reduction of Cr^{6+}

Ling Yu[ab#], Hui Wang[c#], Qi Huang[ab], Hainan Liu[ab], Qingkong Chen[ab], Bojie Yuan[ab], Qi Li[ab], Xiaofei Zhao[ab], Junwang Tang [c], Deqiang Zhao[abc*]

[a]School of River and Ocean Engineering, Chongqing Jiaotong University, Chongqing 400074, China

[b]Key Laboratory of Hydraulic and Waterway Engineering of the Ministry of Education, and National Engineering Research Center for Inland Waterway Regulation, Chongqing, China

[c]Department of Chemical Engineering, University College London, Torrington Place, London WC1E 7JE, U.K.

*Correspondence authors.

[#]These authors contributed equally to this work.

Graphical abstract

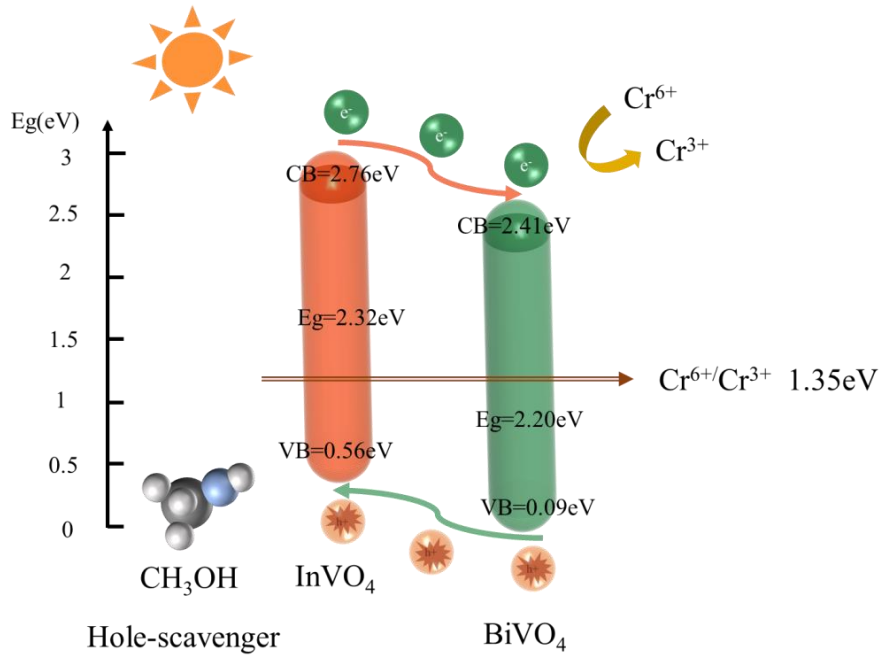

Abstract

A series of $BiVO_4/InVO_4$ composites were synthesized by one-pot microwave method based on the ratio regulation of Bi/In. Consequently, the as-fabricated $BiVO_4/InVO_4$ photocatalysts performed higher photocatalytic activities (100%) than pure $InVO_4$ and $BiVO_4$. The prepared photocatalysts were characterized by X-ray diffraction (XRD), X-ray photoelectron spectroscopy (XPS), transmission electron microscopy (TEM), UV–vis diffuse reflection spectroscopy (UV-vis DRS) and Fourier transform infrared spectra (FTIR). The results indicate the formation of $BiVO_4/InVO_4$ and it possesses enhanced solar light absorption. The enhanced reduction rate is ascribed to the efficient separation of photogenerated charge carriers due to the heterojunction formed between $BiVO_4$ and $InVO_4$. The possible photocatalytic mechanism of $BiVO_4/InVO_4$ composite was also discussed in detail.

Keywords: $BiVO_4$, $InVO_4$, heterojunction, Cr^{6+} reduction, photocatalytic activity.

1. Introduction

Chromium is the seventh most abundant element on the earth and is mainly mined in the form of chromite ($FeCr_2O_4$) ore (Cervantes and Campos-García, 2007; Sivaranjanee and Saravanan, 2018). Chromium plays an important role in industrial material and is widely used in electroplating, ferroalloy products, leather manufacturing, fuels and chemical products. Cr^{6+} has been classified as a class A carcinogen by the U.S. Environmental Protection Agency (EPA), with high solubility and mobility in aqueous solutions, difficulty in biodegradation and enrichment in animal and human tissues through the food chain. According to pH and concentration, Cr^{6+} mainly exists in the form of $Cr_2O_7^{2-}$, $HCrO^{4-}$ and CrO_4^{2-} (Miretzky and Cirelli, 2010; Sultana et al., 2014). Compared with Cr^{6+}, Cr^{3+} is more stable, and Cr^{3+} is an essential trace element for human body. Photocatalysis has been seen as a green route to convert Cr^{6+} to Cr^{3+} in aqueous media (Mao et al., 2016; Zhang et al., 2011; Zhao et al., 2021a). However, most photocatalysts still suffer from limited light absorption and especially the rapid recombination of photo-induced charge carriers (Cheng et al., 2021).

In recent years, Bi-based photocatalysts have been extensively studied (Yang et al., 2019), especially $BiVO_4$ due to the characteristics of wide range of component elements, good chemical properties and thermal stability in aqueous solution (Kim and Choi, 2014; Rao et al., 2014; Wang et al., 2020b). Hence, it has been reported to effectively use solar energy for pollutants removal (Wang et al., 2020a; Yang et al., 2020b). Chala (Chala et al., 2014) prepared pure $BiVO_4$ and 0.5 ~ 5.0mol% Fe loaded $BiVO_4$ samples by a hydrothermal method. The results clearly showed that Fe-loaded $BiVO_4$ sample exhibited remarkably higher activity than pure $BiVO_4$. Shi (Shi et al., 2017) showed that a novel bismuth vanadate-palygorskite ($BiVO_4$-Pal) photocatalyst exhibits photocatalytic activity for tetracycline hydrochloride removal under visible light. The pseudo-first-order degradation rate constant for $BiVO_4$-Pal composites was approximately 2.1 times higher than that of pure $BiVO_4$, and the photodegradation rate of the

$BiVO_4$-Pal composite was 1.4 times greater than that of pure $BiVO_4$. However, low surface adsorption capacity and rapid charge recombination were the two main reasons for limiting its application. In order to solve this problem, many methods such as metal ion deposition, non-metal doping have been adopted (Yang et al., 2020a). Noteworthy, two or more semiconductors are combined to form a heterojunction, which promotes the separation of photogenic carriers and provides additional active sites for photocatalytic reactions (Li et al., 2022; Sun et al., 2018; Zhao et al., 2021b). Many studies have shown that $InVO_4$ can enhance the photocatalytic degradation efficiency of organic pollutants under visible light irradiation (Lin et al., 2015). Based on the narrow band gap of $InVO_4$ (Eg = 1.9 eV) and $BiVO_4$ (Eg = 2.4 eV), combining $BiVO_4$ and $InVO_4$ to form a type II staggered heterojunction is an effective route (Zhang et al., 2019). Besides, $BiVO_4$/$InVO_4$ heterojunction allows photogenerated carriers to migrate from one semiconductor to another through the interface, thereby promoting photocatalytic property (Fang et al., 2022; Mu et al., 2022; Wang et al., 2021; Wang et al., 2022; Yang et al., 2020a).

In this work, $BiVO_4$/$InVO_4$ heterojunction was obtained by one-pot microwave strategy. The suitable band structures between $BiVO_4$ and $InVO_4$ make it possible to form a heterojunction, allowing it to possess enhanced light absorption and charge transport, which was beneficial to the improvement of photocatalytic activity The physical and chemical properties of the heterojunction were analyzed by XRD, SEM, FTIR, X- XPS and UV-vis spectroscopy. The photocatalytic performance of the samples was evaluated by the reduction of Cr^{6+} under visible light irradiation. This study demonstrates that combining $BiVO_4$ and $InVO_4$ to form $BiVO_4$/$InVO_4$ heterojunction is a feasible scheme for exploiting photocatalytic degradation of hexavalent chromium.

2 Materials and Methods

2.1 Materials and Reagents

The materials included analytical grade pure bismuth nitrate ($Bi(NO_3)_3·5H_2O$, Alfa Aesar), analytical grade pure sodium hydroxide powder (NaOH, SIGMA-ALDRICH), analytical grade pure bismuth nitrate ($In(NO_3)_3$·SIGMA-ALDRICH,), ammonium metavanadate (NH_4VO_3, SIGMA-ALDRICH), nitric acid(HNO_3, SIGMA-ALDRICH), Potassium chromate (K_2CrO_4, SIGMA-ALDRICH), Sulfuric acid(H_2SO_4, SIGMA-ALDRICH), Methyl alcohol($C_2H_6O_2$, Fisher Scientific), phosphoric acid(H_3PO_4, SIGMA-ALDRICH), citric acid($C_6H_8O_7$, Fisher Scientific), which were purchased from Aladdin.

2.2 Synthesis of Photocatalysts

One-pot microwave strategy was used to prepare $BiVO_4/InVO_4$, as presented in Scheme 1. In detail, 2 mmol $Bi(NO_3)_3·5H_2O$ and $In(NO_3)_3·XH_2O$ with various molar ratio were dissolved in 4 mL of 4 mol/L HNO_3, followed by the addition of 50 mL of deionized water to form solution A. Similarly, 2 mmol NH_4VO_3 was dissolved in 4 mL of 4 mol/L NaOH to form solution B. Finally, solution B was mixed to solution A, and then transferred the mixed solution to a PTFE standard tank for the microwave reaction at 160℃ (with a ramp of 25 min) for 40 min (power 120W). The mixed solution was allowed to cool to room temperature. The obtained precipitate was further rinsed until a pH of ~7, and then dried at 60℃ for 24 h in vacuum. The obtained samples with expected $Bi(NO_3)_3·5H_2O/In(NO_3)_3·XH_2O$ ratio of 0.75:0.25;0.5:0.5;0.25:0.75 were labeled as 0.75 $BiVO_4$/0.25 $InVO_4$, 0.5 $BiVO_4$/0.5 $InVO_4$, 0.25 $BiVO_4$/0.75 $InVO_4$, $BiVO_4$, samples. As reference, normal $InVO_4$ and $BiVO_4$ were synthesized via the same strategy but without the introduction of NH_4VO_3 and $In(NO_3)_3·XH_2O$.

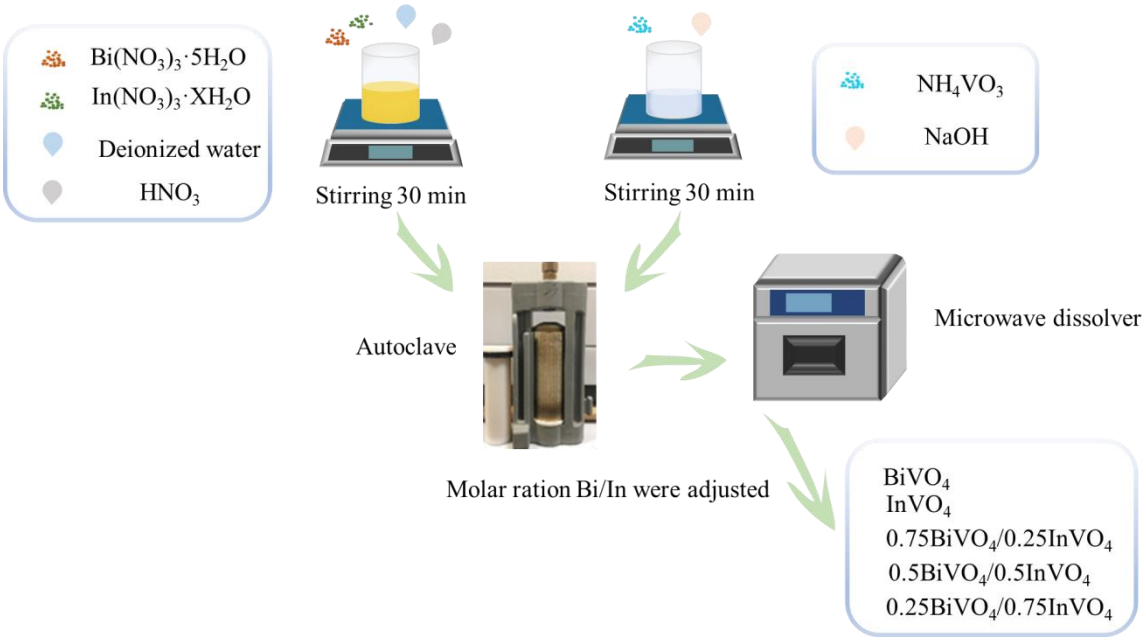

Scheme.1. schematic illustration for the preparation of $InVO_4$, 0.75 $BiVO_4$/0.25 $InVO_4$, 0.5 $BiVO_4$/0.5 $InVO_4$, 0.25 $BiVO_4$/0.75 $InVO_4$, $BiVO_4$, samples.

2.3 Characterization

The crystal structures of prepared samples were characterized using X-ray diffraction (XRD) under Mo Kα radiation with a Rigaku D/Max2500pc (Tokyo, Japan) diffractometer (scanning angle 2θ from 0◦ to 40◦, and scanning rate of 4◦/min). A high-voltage (10 kV) Tescan FEG-SEM microscope (TESCAN, MARI3, Brno, Czech Republic) was used to acquire scanning electron microscopy (SEM) images of the prepared samples. Transmission electron microscopic (TEM) images of the prepared samples were obtained by the JEM-2100F equipment (operating at 200kV). The chemical characteristics of sample surfaces were investigated using X-ray photoelectron spectra (XPS) acquired with a PHI5000 (ULVAC-PHI, INC, Kanagawa Prefecture, Japan) versa probe system under monochromatic Al K X-rays. The visible light source was a 300 W Xe lamp (with a <420 nm UV cutoff filter), and all experiments were carried out at room temperature. UV–vis absorbance spectra of the as-prepared samples were recorded with Solid Spec-3700/3700 DUV (Tokyo, Japan) in the range of 200–800 nm. Fourier transform infrared spectra (FTIR) of the samples were collected from IRAffinity-1S FTIR spectrometer in the range of 600–4000 cm^{-1}.

2.4 Evaluation of Photocatalytic Activity Based on Cr^{6+} Reduction

The photocatalytic reduction of Cr^{6+} was conducted as follows. 0.01g catalyst was added to 25ml of 10mg/L Cr^{6+} solution (prepared with K_2CrO_4), the pH value of which was adjusted to 4.2 using the H_2SO_4 solution followed by introducing methanol as a hole scavenger. The mixed solution was stirred for 1h under dark to achieve adsorption equilibrium, which was seen as the initial concentration (C_0). A 300W Xe lamp with a <420nm cut-off filter was used for photocatalytic reduction, and the solution was measured at defined time intervals. In detail, 1mL of the reaction solution was diluted to 50 mL. Then 1:1 phosphoric acid and sulfuric acid solution were added to diphenyl carbazide (diphenyl carbazide, DPC), and then the final colored solution was measured at 540 nm by spectrophotometer (UV 3000).

3 Results and discussion

3.1 Morphological studies

Fig.1a and b show SEM images of $BiVO_4$ sample, which presents a cluster structure consisted of several long rice grain particles accumulations with rough surface and an average diameter about 2 μm. The morphology of pure $InVO_4$ (Fig.1c and d) demonstrates the bulb-like particles with an average diameter of 1 μm. Interestingly, the morphology and size of the $BiVO_4/InVO_4$ are totally different to the pristine, demonstrating a leaf-like nanostructure (Fig.1e and f). This shows the formation of the hybrid $BiVO_4/InVO_4$. To further confirm the heterojunction structure between $BiVO_4$ and $InVO_4$, 0.75 $BiVO_4$/0.25 $InVO_4$ sample was studied by a high resolution transmission electron microscopy (HRTEM), as shown in Fig.2. Fig.2a clearly shows leaf-like nanostructure of $BiVO_4/InVO_4$. From the Fig.2.b, the resolved interplanar distances of $BiVO_4$ and $InVO_4$ are about 0.23 and 0.258 nm, corresponding to the (121) plane of $BiVO_4$ and the (022) plane of $InVO_4$, respectively. The observed interconnection demonstrates the formation of $BiVO_4/InVO_4$ heterojunction, which was further confirmed by the elemental mapping (Fig.2e–i), where In, V, Bi, and O elements are uniformly dispersed in the obtained leaf-like nanostructure.

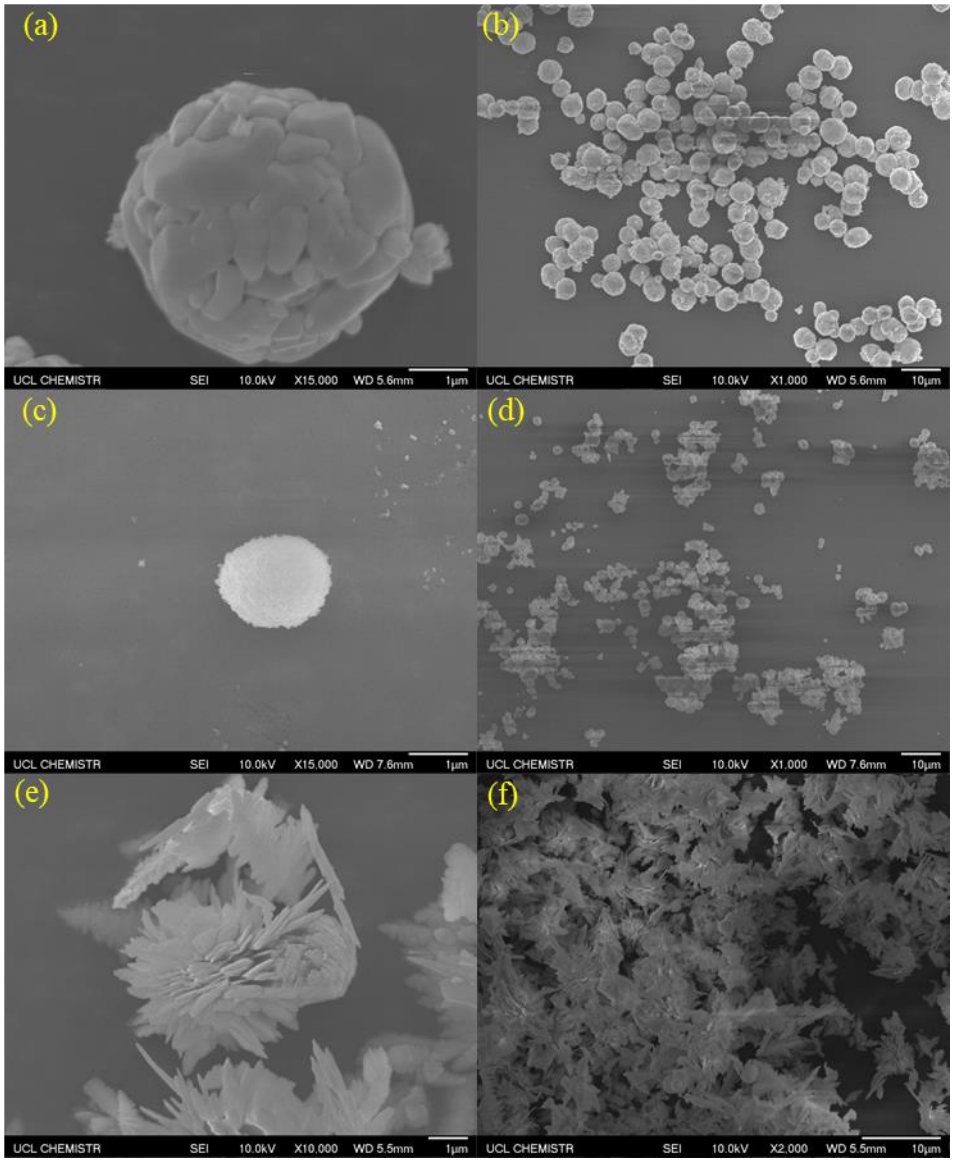

Fig.1. SEM images of the as-synthesized samples: **(a)** and **(b)** $BiVO_4$, **(c)** and **(d)** $InVO_4$, **(e)** and **(f)** 0.75 $BiVO_4$/0.25 $InVO_4$

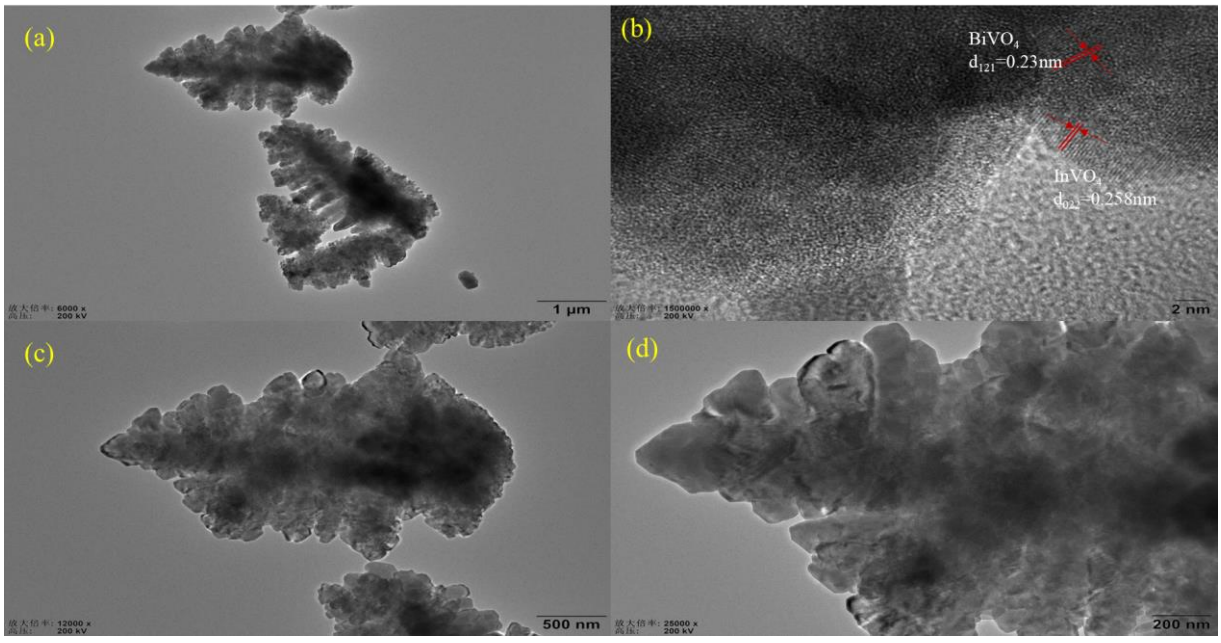

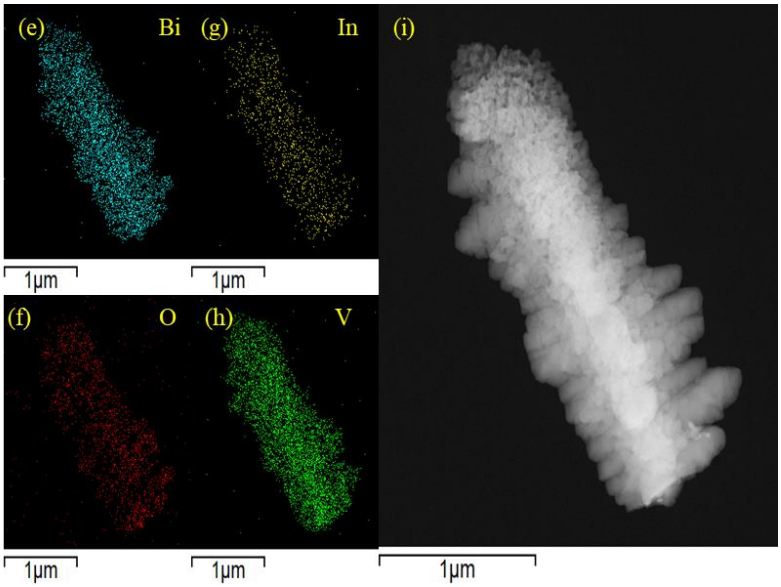

Fig.2. TEM image **(a, c and d)**, HRTEM image **(b)**, and the corresponding EDS elemental mapping images of 0.75 $BiVO_4$/0.25 $InVO_4$ **(e–i)**.

3.2 Structural analysis

The purity and crystallinity of the samples was analyzed by the X-ray diffraction (XRD). Fig.3 shows the XRD patterns of $InVO_4$, 0.75 $BiVO_4$/0.25 $InVO_4$, 0.5 $BiVO_4$/0.5 $InVO_4$, 0.25 $BiVO_4$/0.75 $InVO_4$, $BiVO_4$ samples. $BiVO_4$ exhibits peaks at 2θ angles of 8.6°, 13°, 16°, 21.5°, 27°, which are consistent with the XRD standard card of the monoclinic system $BiVO_4$ (PDF#78-1534). $InVO_4$ presents the characteristic peaks at 8.5°, 15°, 15.9°, 21°, 27.2°, matching well with the XRD standard card of orthorhombic $InVO_4$ (PDF#71-1689). When introducing 0.25 $BiVO_4$ in $InVO_4$, the peaks of $InVO_4$ remain but exhibit slight shifts. Such the change of signals may be attributed to that $InVO_4$ may not crystallize well due to the adding of $BiVO_4$. With the increasing content of $BiVO_4$, the XRD pattern of $BiVO_4$/$InVO_4$ tends to be similar to the pristine $BiVO_4$ and $InVO_4$. XRD and morphology results indicate the formation of $BiVO_4$/$InVO_4$ heterojunction. The XRD patterns were analyzed by Rietveld refinement using the Maud 2.80 software. We can see from Fig.4 that the final calculation result of the mass percentage of $BiVO_4$ is 78.19% and $InVO_4$ is 21.81% (Cao et al., 2020; Lutterotti, 2010).

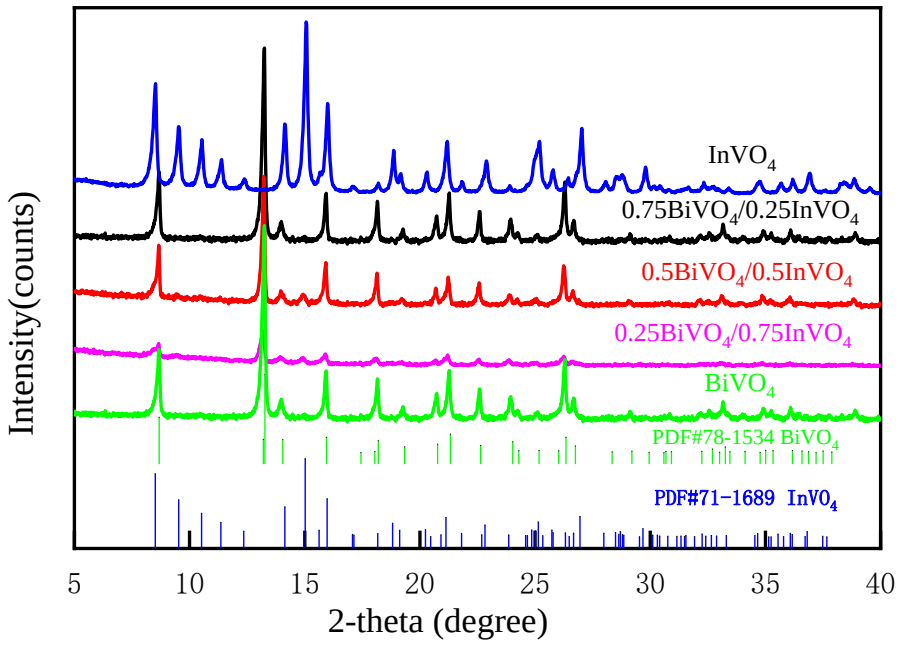

Fig.3. XRD diffraction patterns of $InVO_4$, 0.75 $BiVO_4$/0.25 $InVO_4$, 0.5 $BiVO_4$/0.5 $InVO_4$, 0.25 $BiVO_4$/0.75 $InVO_4$, $BiVO_4$ samples.

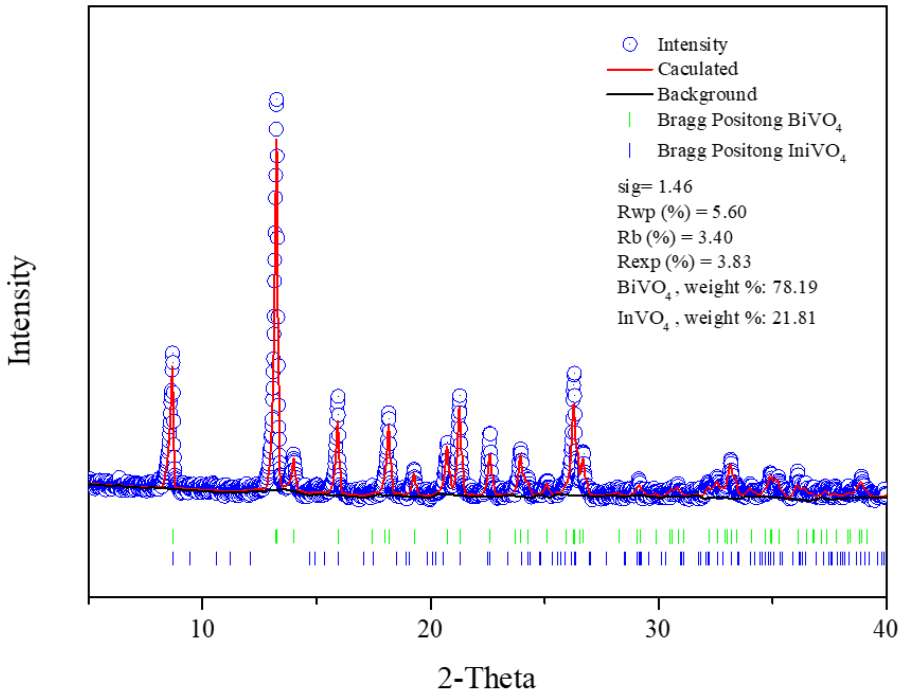

Fig.4 Rietveld refinement of 0.75$BiVO_4$/0.25$InVO_4$.

The FT-IR spectra of the obtained samples are shown in Fig.5, and the signals of pure $BiVO_4$ and $InVO_4$ match well with the earlier reports (Liu et al., 2016; Regmi et al., 2018; Shi et al., 2014). For $BiVO_4$, the peaks at 710 cm^{-1} and 810 cm^{-1} may be due to V-O symmetric and asymmetric stretching vibrations. The characteristic peak at 617 cm^{-1} is ascribed to Bi-O vibration. For $InVO_4$, the characteristic peak at 956 cm^{-1} may be due to V-O symmetric and asymmetric stretching vibrations. The peaks at 903 and 756 cm^{-1} belong to the vibration modes

of V–O–In. The characteristic peak at 717 cm^{-1} could be ascribed to VO_4^{3-}(Faisal et al., 2021). For the 0.75 $BiVO_4$/0.25 $InVO_4$ composites, the characteristic peaks at various positions are detected, where 898 cm^{-1} could be attributed to In-O vibration and 679 cm^{-1} may be ascribed to the vibration of V-O, suggesting that the formation of the hybrid $BiVO_4$/$InVO_4$.

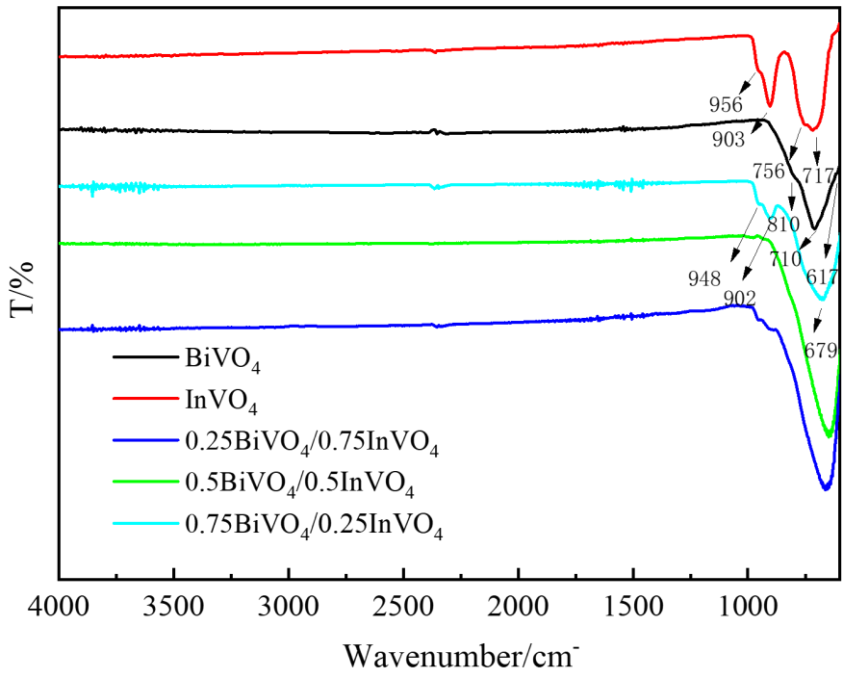

Fig.5. FT-IR spectra of $InVO_4$, 0.75 $BiVO_4$/0.25 $InVO_4$, 0.5 $BiVO_4$/0.5 $InVO_4$, 0.25 $BiVO_4$/0.75 $InVO_4$, $BiVO_4$ samples.

The XPS was performed to study the surface elemental composition and electronic structure of the prepared samples. Fig.6a exhibits the XPS spectra of $InVO_4$, 0.75 $BiVO_4$/0.25 $InVO_4$, 0.5 $BiVO_4$/0.5 $InVO_4$, 0.25 $BiVO_4$/0.75 $InVO_4$, $BiVO_4$, which manifests the existence of In, Bi, V and O elements of the hybrid samples. Given the carbon element in the air, C 1s characteristic peaks are observed (Lin et al., 2013). As presented in Fig.6b, In 3d is composed of two peaks situated at 445.2 eV and 452.6 eV in $InVO_4$, 445.2 eV and 452.5 eV in 0.25 $BiVO_4$/0.75 $InVO_4$, 445.2 eV and 452.5 eV in 0.5 $BiVO_4$/0.5 $InVO_4$ and 445 eV and 452 eV in 0.75 $BiVO_4$/0.25 $InVO_4$, which are due to In^{3+}(Min et al., 2012), in addition, Bi 4d peak located at 442.2 eV in 0.75 $BiVO_4$/0.25 $InVO_4$, 442.6 eV in 0.5 $BiVO_4$/0.5 $InVO_4$ and 442.5 eV in 0.25 $BiVO_4$/0.75 $InVO_4$ appears (Lakhera et al., 2019) It can be seen that the characteristic peaks of Bi 4f located at 158.7 eV and 164.5 eV in $BiVO_4$, 159 eV and 164.7 eV in 0.25 $BiVO_4$/0.75 $InVO_4$, 159.2 eV and 164.6 eV 0.5 $BiVO_4$/0.5 $InVO_4$ and 158.7 eV and 164.5 eV in 0.75 $BiVO_4$/0.25 $InVO_4$, are attributed to Bi^{3+}(Wu et al., 2013), from Fig.6c. Fig. 6d shows the XPS spectra of V 2p and O

1s orbital in $InVO_4$, 0.75 $BiVO_4$/0.25 $InVO_4$, 0.5 $BiVO_4$/0.5 $InVO_4$, 0.25 $BiVO_4$/0.75 $InVO_4$, $BiVO_4$. The V 2p peaks are located at 517 eV and 524.9 eV in $BiVO_4$, 517.8 eV 525.2 eV in $InVO_4$, 517.4 eV and 524.9 eV in 0.25 $BiVO_4$/0.75 $InVO_4$, 517.4 eV and 524.9 eV 0.5 $BiVO_4$/0.5 $InVO_4$ and 517 eV and 524.9 eV in 0.75 $BiVO_4$/0.25 $InVO_4$, which could be due to the surface V^{5+} of $BiVO_4$ and $InVO_4$(Min et al., 2012). The O 1s peaks are situated at approximately 530 eV,530 eV and 532 eV in $BiVO_4$, $InVO_4$, 0.25 $BiVO_4$/0.75 $InVO_4$, 0.5 $BiVO_4$/0.5 $InVO_4$ 0.75 $BiVO_4$/0.25 $InVO_4$, ascribable to the chemisorbed water, oxygen in metal oxide lattice and hydroxyl groups (Li et al., 2015; Li et al., 2008). Obviously, the XPS spectra of 0.5 $BiVO_4$/0.5 $InVO_4$ and 0.75 $BiVO_4$/0.25 $InVO_4$ composite film shifts to higher wavelength, indicating the combination of $BiVO_4$ and $InVO_4$ heterojunction was very successful.

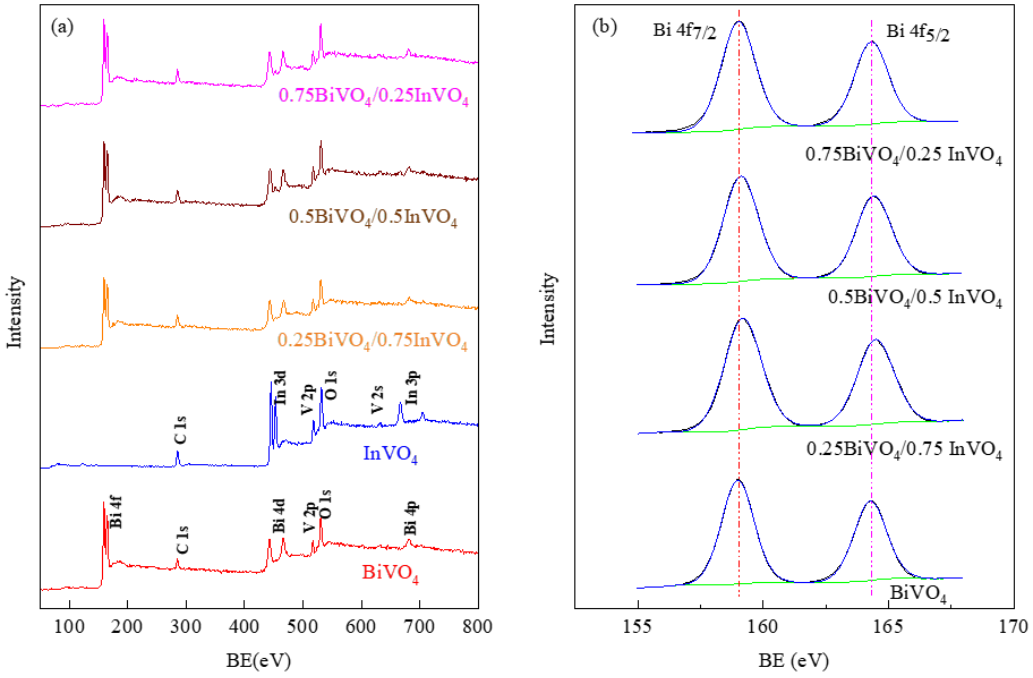

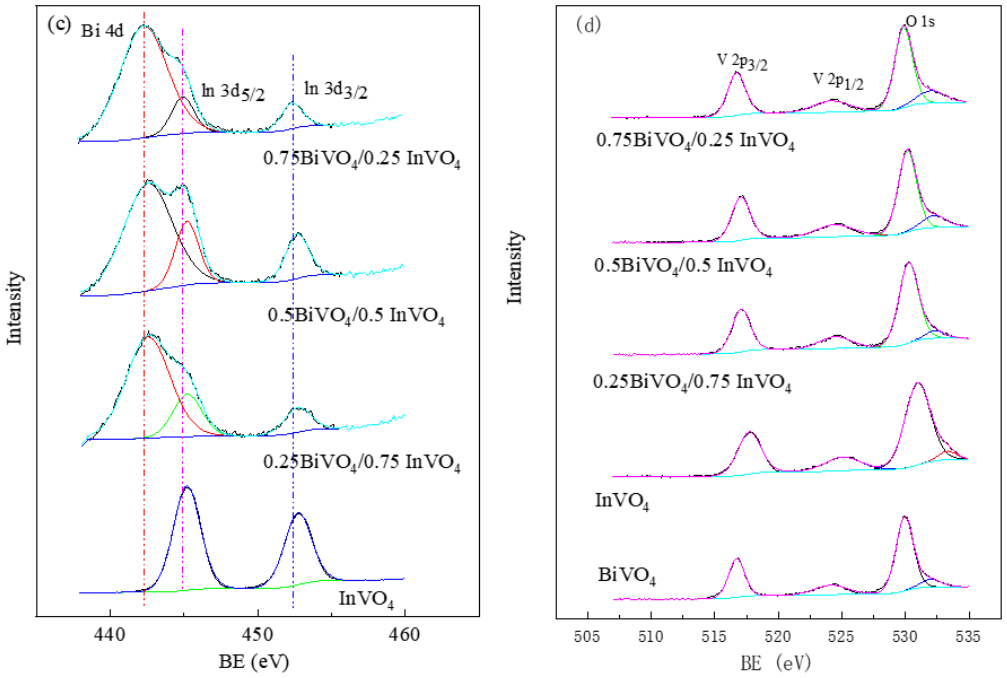

Fig.6. XPS spectra **survey**, **(a), (b)** and **(c)** of $InVO_4$, 0.75 $BiVO_4$/0.25 $InVO_4$, 0.5 $BiVO_4$/0.5 $InVO_4$, 0.25 $BiVO_4$/0.75 $InVO_4$, $BiVO_4$, samples.

UV–vis spectroscopy was performed to study the electronic structure of semiconductors. The UV–vis diffuse reflectance spectra of the samples, displayed in Fig.7a. The absorption edges of pure $InVO_4$ and $BiVO_4$ are at approximately 490 and 530 nm, respectively, in agreement with the published (Cheng et al., 2017; Meng et al., 2017). Comparatively, the adsorption edge of $BiVO_4$/$InVO_4$ heterojunction shows a significant red shift and enhanced the response of visible light. Particularly, 0.75 $BiVO_4$/0.25 $InVO_4$ shows the strongest absorbance in the visible light region, which might be helpful for the photocatalytic reaction. Further, the band gap energies of as-prepared samples were determined by Mott-Schottky plot. The absorption coefficient α and direct band gap Eg of $InVO_4$ and $BiVO_4$ are related to the following equation: $\alpha hv = A_0(hv - E_g)^{n/2}$ (Hu et al., 2015), where α, A_0, Eg and hν demonstrate the absorption coefficient, the constant, the direct band gap energy and incident photon energy, respectively. Among these parameters, n is determined by the type of optical transition of a semiconductor (n=1 for a direct transition and n=4 for an indirect transition). For $InVO_4$ and $BiVO_4$, the value of n is 1 for the direct transition. The band gap energy of pure $BiVO_4$ and $InVO_4$ nanocomposite were depicted in Fig.7b. According to the equation, the band gap energy of $BiVO_4$ nanocomposites is 2.20 eV, which is smaller than that of the pure $InVO_4$ particles (2.32 eV).

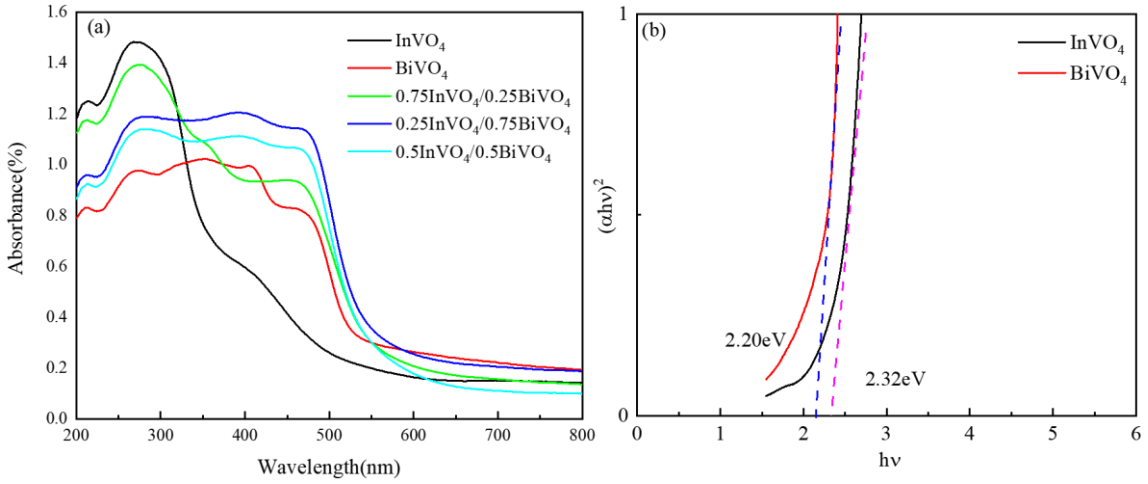

Fig.7. (a) UV-Vis diffuse reflectance spectra of $InVO_4$, 0.75 $BiVO_4$/0.25 $InVO_4$, 0.5 $BiVO_4$/0.5 $InVO_4$, 0.25 $BiVO_4$/0.75 $InVO_4$, $BiVO_4$, samples. **(b)** plots of $(ahv)^2$ vs. photon energy (hv)for the band gap energies of $InVO_4$ and $BiVO_4$.

3.3 Photocatalytic activity

As shown in the Fig.8a, the photocatalytic performance of the samples were tested by reduction of Cr^{6+} within 60 min of dark adsorption and 40 min under visible light irradiation. The control experiment without adding any catalyst was carried out, and only the ignorable fluctuation of Cr^{6+} concentration is observed. The dark adsorption efficiency of all samples is less than 10%. Under visible light irradiation, the Cr^{6+} reduction efficiency of pure $BiVO_4$ and $InVO_4$ are improved to be 41% and 56.39% respectively within 40 min. The 0.75 $BiVO_4$/0.25 $InVO_4$ catalyst exhibits the highest photocatalytic activity, and the Cr^{6+} reduced to Cr^{3+} completely within 40 min. The efficiency of 0.5 $BiVO_4$/0.5 $InVO_4$ and 0.25 $BiVO_4$/0.75 $InVO_4$ are 71.6% and 46.81%, respectively after 40 min. From Fig.8c, the absorption peak intensity of Cr^{6+} were drastically decreased and finally disappear, suggesting complete reduction of toxic Cr^{6+} to Cr^{3+} within 40 min. In addition, as exhibited in the Fig.8d, the color of the reaction solution becomes lighter with irradiation time increasing. The solution was completely transparent liquid after 60 min. The photocatalytic reduction kinetics could be depicted by pseudo-first-order kinetics equation (Xing et al., 2017): $-\ln(C/C_0) = kt$, where k is the apparent rate constant, C and C_0 are concentrations of Cr^{6+}, corresponding to time t and t_0 respectively. As presented in Fig.8b, it can be confirmed that the apparent rate constants of pure $InVO_4$ and $BiVO_4$ were 0.033 min^{-1} and 0.011 min^{-1}, respectively. Nevertheless, the apparent rate constants of 0.75 $BiVO_4$/0.25 $InVO_4$,

0.5 $BiVO_4$/0.5 $InVO_4$, 0.25 $BiVO_4$/0.75 $InVO_4$ were 0.089 min^{-1}, 0.015 min^{-1} and 0.016 min^{-1} respectively. It is obvious that the photocatalytic reduction performance for Cr^{6+} of 0.75 $BiVO_4$/0.25 $InVO_4$ is the best among these as-prepared samples.

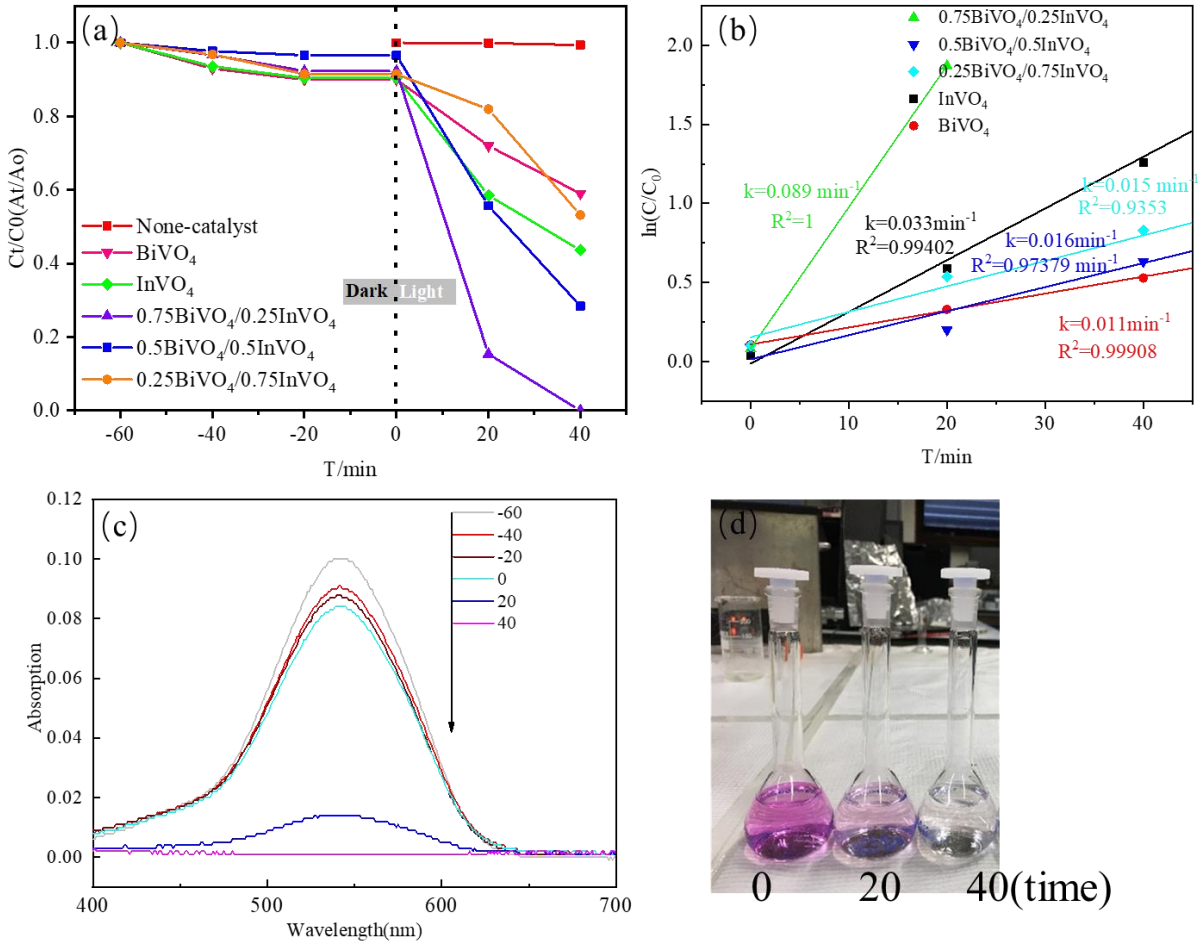

Fig.8. (a) Photocatalytic reduction of Cr^{6+} with $InVO_4$, 0.75 $BiVO_4$/0.25 $InVO_4$, 0.5 $BiVO_4$/0.5 $InVO_4$, 0.25 $BiVO_4$/0.75 $InVO_4$, $BiVO_4$, samples. **(b)** Kinetics plots for photocatalytic reduction of Cr^{6+} with $InVO_4$, 0.75 $BiVO_4$/0.25 $InVO_4$, 0.5 $BiVO_4$/0.5 $InVO_4$, 0.25 $BiVO_4$/0.75 $InVO_4$, $BiVO_4$, samples. Photocatalytic reduction of Cr^{6+} to Cr^{3+} in the presence of 0.75 $BiVO_4$/0.25 $InVO_4$ samples. **(c).** Photocatalytic reduction of Cr^{6+} to Cr^{3+} in the presence of 0.75 $BiVO_4$/0.25 $InVO_4$ samples. **(d).** The color rendering of 0.75$BiVO_4$/0.25$InVO_4$, after reduction of Cr^{6+}.

3.4 Proposed photocatalytic mechanism

To explore the mechanism of photocatalytic Cr^{6+} reduction via $BiVO_4$/$InVO_4$, the relative band positions of $BiVO_4$ and $InVO_4$ were studied. According to the equation(Ge et al., 2006; Jiang et al., 2009): $E_{VB} = X + 0.5E_g - E_0$, where the E_{CB} is the potential of conduction band edge, X is the electronegativity of the semiconductor, E_0 is the scale factor that correlates the redox level of the reference electrode with the absolute vacuum (for normal hydrogen electrode (NHE), E_0 = 4.5 eV), and E_g is the band gap energy of the semiconductor. Combined with the following equation: $E_{VB} = E_g + E_{CB}$, the potential of conduction band edge (CB) and valence

band edge (VB) of $BiVO_4$ were calculated to be 0.4 eV and 2.8 eV, respectively, as well as the CB and VB of $InVO_4$ were calculated to be -0.19 eV and 1.71 eV respectively. The electron transfer mechanism is proposed in Fig.9. The CB of $InVO_4$ is more negative than that of the $BiVO_4$, demonstrating that photoinduced electrons could shift from the CB of $InVO_4$ to the CB of $BiVO_4$**,** which is beneficial to charge separation. According to the chromium concentration and pH value, its primary existence form is $HCrO^{4-}$ ($CrO^{4-}+7H^{+}+3e^{-} \rightleftarrows Cr^{3+}+4H_2O$). The theoretical potential of Cr^{6+}/Cr^{3+} is 1.35eV, which is more positive than the CB of $BiVO_4$, allowing the accelerated electrons in $BiVO_4$ thermodynamically reduce Cr^{6+} to Cr^{3+}. Similarly, given that the VB of $InVO_4$ is positive than that of $BiVO_4$, holes are transferred from the VB of $BiVO_4$ to that of $InVO_4$, followed by the elimination of methanol.

Based on the above analysis, the possible photocatalytic mechanism of $BiVO_4/InVO_4$ heterojunction catalyst was proposed. First, $BiVO_4$ and $InVO_4$ semiconductors are excited under visible light to produce photogenerated electron-hole pairs. The h^+ of $BiVO_4$ is migrated to $InVO_4$, while the e^- of $InVO_4$ is migrated to $BiVO_4$. Importantly, the addition of methanol eliminated the holes and inhibited the recombination of electron hole pairs. Finally, e^- participate in the reduction-oxidation reaction. The detailed reaction process is as follows:

$$BiVO_4+hv \rightarrow e^-+h^+ \quad (1)$$

$$InVO_4+hv \rightarrow e^-+h^+ \quad (2)$$

$$Cr^{6+}+e^- \rightarrow Cr^{3+} \quad (3)$$

The main reasons of the excellent performance of $BiVO_4/InVO_4$ heterojunction are following. Firstly, the enhanced light absorption of the hybrid is observed compared with two semiconductors, which helps to capture more photons for the photocatalytic reaction. What's more, the formed heterojunction facilitates the charge separation and transport, allowing the photo-generated electrons to be accelerated for Cr^{6+} reduction.

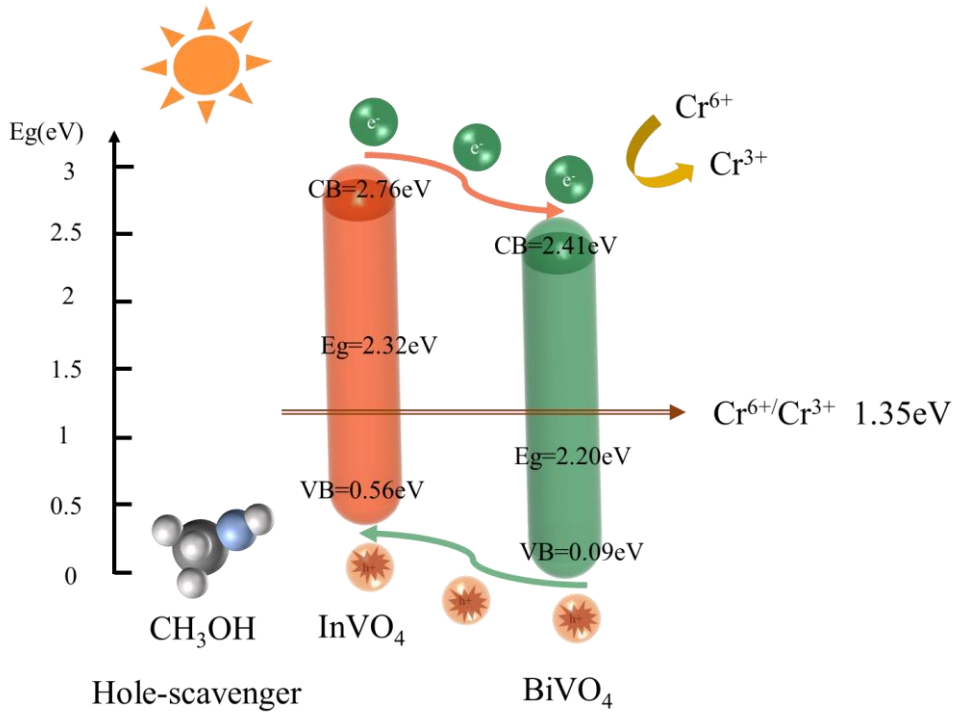

Fig.9. Schematic illustration for the possible photocatalytic mechanism of the 0.75 $BiVO_4$/0.25 $InVO_4$ composite for Cr^{6+} reduction under visible light irradiation.

3.5 Stability and recyclability properties

To investigated the stability and recyclability of 0.75 $BiVO_4$/0.25 $InVO_4$, we have conducted Cr^{6+} reduction efficiency recycling test by 5 times. Figure 10 shows the before and after recycling XRD diffraction patterns of 0.75 $BiVO_4$/0.25 $InVO_4$. The results show that the reduction efficiency of Cr^{6+} tends to be nearly constant over five cycles. In the repeated tests, the reduction efficiency after each cycle is maintained at 100%. In addition, the phase structures of the sample remain unchanged, which verifies that the components of the 0.75 $BiVO_4$/0.25 $InVO_4$. are difficult to be photo-decomposed and its structure is stable during the photocatalytic process. This feature is very important for its practical application and modification.

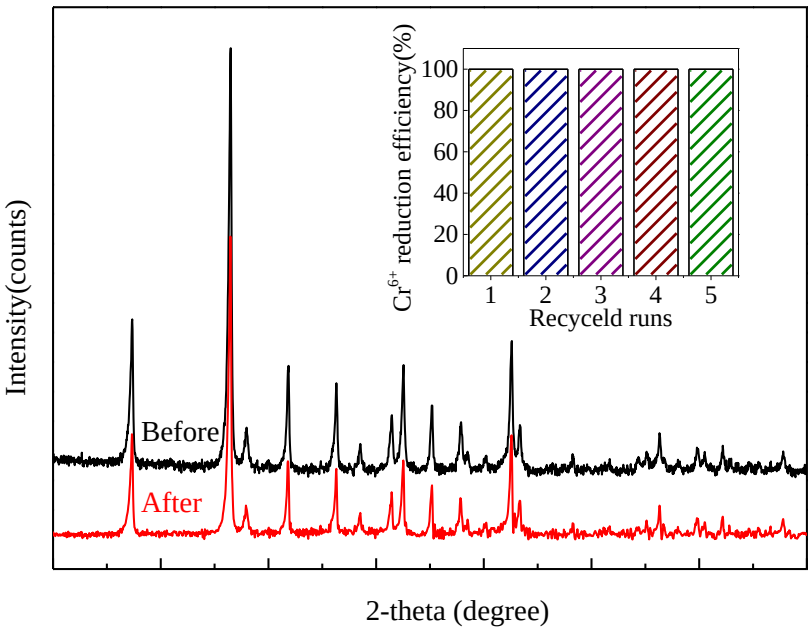

Fig.10 Before and after recycling XRD diffraction patterns of 0.75 $BiVO_4$/0.25 $InVO_4$ and Cr^{6+} reduction efficiency as inset

4 Conclusions

In summary, a green conversion from Cr^{6+} to Cr^{3+} has been presented using $BiVO_4/InVO_4$ heterojunction that was obtained using a one-pot microwave strategy. The optimized sample exhibited the degradation rate of almost 100% in 40min, which was 2 times higher than that of $BiVO_4$ and $InVO_4$. The high photocatalytic performance could be ascribed to the thin leaf-like structure of $BiVO_4/InVO_4$ heterojunction, strong visible light absorption and more importantly hinders the recombination of photo-generated charge carries.

Acknowledgements

This work was supported by the Science and Technology Research Program of Chongqing Municipal Education Commission (Grant No. KJQN202100739), Natural Science Foundation of Chongqing, China (Grant No. cstc2021jcyj-msxmX0912), the Foundation for High-level Talents of Chongqing Jiaotong University (19JDKJC-C023 , 20JDKIC-A042) and China Schoolar Council (CSC).

Author contributions

Deqiang Zhao (Corresponding Author): Conceptualization, Methodology, Software, Investigation, Formal Analysis;

Ling Yu (First Author): Data Curation, Writing - Original Draft;

Hui Wang: Conceptualization, Funding Acquisition, Resources, Supervision, Writing - Review & Editing;

Qi Huang: Visualization, Investigation;

Hainan Liu: Data Curation, Investigation;

Qingkong Chen: Software, Validation;

Bojie Yuan: Visualization, Writing - Review & Editing;

Qi Li: Resources, Supervision;

Xiaofei Zhao: Conceptualization, Resources;

Junwang Tang: Supervision, Writing - Review & Editing.

References

Cao, Y., Xia, X., Liu, Y., Wang, N., Zhang, J., Zhao, D., Xia, Y., 2020. Scalable synthesizing nanospherical $Na4Fe_3(PO4)_2(P_2O_7)$ growing on MCNTs as a high-performance cathode material for sodium-ion batteries. Journal of Power Sources 461, 228130.

Cervantes, C., Campos-García, J., 2007. Reduction and efflux of chromate by bacteria, Molecular microbiology of heavy metals. Springer, pp. 407-419.

Chala, S., Wetchakun, K., Phanichphant, S., Inceesungvorn, B., Wetchakun, N., 2014. Enhanced visible-light-response photocatalytic degradation of methylene blue on Fe-loaded $BiVO_4$ photocatalyst. Journal of Alloys and Compounds 597, 129-135.

Cheng, C., Fang, Q., Fernandez-Alberti, S., Long, R., 2021. Controlling Charge Carrier Trapping and Recombination in $BiVO_4$ with the Oxygen Vacancy Oxidation State. The Journal of Physical Chemistry Letters 12, 3514-3521.

Cheng, J., Yan, X., Mo, Q., Liu, B., Wang, J., Yang, X., Li, L., 2017. Facile synthesis of g-C_3N_4/$BiVO_4$ heterojunctions with enhanced visible light photocatalytic performance. Ceramics International 43, 301-307.

Faisal, M., Iqbal, A., Adam, F., Jothiramalingam, R., 2021. Effect of Cu doping on the photocatalytic activity of $InVO_4$ for hazardous dye photodegradation under LED light irradiation and its mechanism. Water Science and Technology.

Fang, B., Xing, Z., Kong, W., Li, Z., Zhou, W., 2022. Electron spin polarization-mediated charge separation in Pd/CoP@ CoNiP superstructures toward optimized photocatalytic performance. Nano Energy 101, 107616.

Ge, L., Xu, M., Fang, H., 2006. Preparation and characterization of silver and indium vanadate co-doped TiO_2 thin films as visible-light-activated photocatalyst. Journal of sol-gel science and technology 40, 65-73.

Hu, L., Dong, S., Li, Q., Li, Y., Pi, Y., Liu, M., Han, X., Sun, J., 2015. Effects of sodium dodecyl benzene sulfonate on the crystal structures and photocatalytic performance of ZnO powders prepared by hydrothermal method. Journal of Alloys and Compounds 649, 400-408.

Jiang, H.-q., Endo, H., Natori, H., Nagai, M., Kobayashi, K., 2009. Fabrication and efficient photocatalytic degradation of methylene blue over CuO/$BiVO_4$ composite under visible-light irradiation. Materials Research Bulletin 44, 700-706.

Kim, T.W., Choi, K.-S., 2014. Nanoporous $BiVO_4$ photoanodes with dual-layer oxygen evolution catalysts for solar water splitting. Science 343, 990-994.

Lakhera, S.K., Hafeez, H.Y., Venkataramana, R., Veluswamy, P., Choi, H., Neppolian, B., 2019. Design of a highly efficient ternary AgI/rGO/$BiVO_4$ nanocomposite and its direct solar light induced photocatalytic activity. Applied Surface Science 487, 1289-1300.

Li, J., Zhao, W., Guo, Y., Wei, Z., Han, M., He, H., Yang, S., Sun, C., 2015. Facile synthesis and high activity of novel $BiVO_4$/$FeVO_4$ heterojunction photocatalyst for degradation of metronidazole. Applied Surface Science 351, 270-279.

Li, Y., Zhang, H., Guo, Z., Han, J., Zhao, X., Zhao, Q., Kim, S.-J., 2008. Highly efficient visible-light-induced photocatalytic activity of nanostructured AgI/TiO_2 photocatalyst. Langmuir 24, 8351-8357.

Li, Z., Li, H., Wang, S., Yang, F., Zhou, W., 2022. Mesoporous black TiO_2/MoS_2/Cu_2S hierarchical tandem heterojunctions toward optimized photothermal-photocatalytic fuel production. Chemical Engineering Journal 427, 131830.

Lin, H., Ye, H., Xu, B., Cao, J., Chen, S., 2013. Ag_3PO_4 quantum dot sensitized $BiPO_4$: A novel p–n junction Ag_3PO_4/$BiPO_4$ with enhanced visible-light photocatalytic activity. Catalysis Communications 37, 55-59.

Lin, X., Guo, X., Shi, W., Zhao, L., Yan, Y., Wang, Q., 2015. Ternary heterostructured Ag–$BiVO_4$/$InVO_4$ composites: Synthesis and enhanced visible-light-driven photocatalytic activity. Journal of Alloys and Compounds 635, 256-264.

Liu, Z., Lu, Q., Guo, E., Liu, S., 2016. Electrospinning synthesis of $InVO_4$/$BiVO_4$ heterostructured nanobelts and their enhanced photocatalytic performance. Journal of Nanoparticle Research 18, 1-11.

Lutterotti, L., 2010. Total pattern fitting for the combined size–strain–stress–texture determination in thin film diffraction. Nuclear Instruments and Methods in Physics Research Section B: Beam Interactions with Materials and Atoms 268, 334-340.

Mao, M., Chen, F., Zheng, C., Ning, J., Zhong, Y., Hu, Y., 2016. Facile synthesis of porous Bi_2O_3-$BiVO_4$ pn heterojunction composite microrods with highly efficient photocatalytic degradation of phenol. Journal of Alloys and Compounds 688, 1080-1087.

Meng, Y., Hong, Y., Huang, C., Shi, W., 2017. Fabrication of novel Z-scheme $InVO_4$/CdS heterojunctions with efficiently enhanced visible light photocatalytic activity. CrystEngComm 19, 982-993.

Min, Y., Zhang, K., Chen, Y., Zhang, Y., 2012. Sonodegradation and photodegradation of methyl orange by $InVO_4$/TiO_2 nanojunction composites under ultrasonic and visible light irradiation. Ultrasonics sonochemistry 19, 883-889.

Miretzky, P., Cirelli, A.F., 2010. Cr (VI) and Cr (III) removal from aqueous solution by raw and modified

lignocellulosic materials: a review. Journal of hazardous materials 180, 1-19.
Mu, F., Miao, X., Cao, J., Zhao, W., Yang, G., Zeng, H., Li, S., Sun, C., 2022. Integration of plasmonic effect and S-scheme heterojunction into gold decorated carbon nitride/cuprous oxide catalyst for photocatalysis. Journal of Cleaner Production 360, 131948.
Rao, P.M., Cai, L., Liu, C., Cho, I.S., Lee, C.H., Weisse, J.M., Yang, P., Zheng, X., 2014. Simultaneously efficient light absorption and charge separation in WO_3/$BiVO_4$ core/shell nanowire photoanode for photoelectrochemical water oxidation. Nano letters 14, 1099-1105.
Regmi, C., Dhakal, D., Lee, S.W., 2018. Visible-light-induced Ag/$BiVO_4$ semiconductor with enhanced photocatalytic and antibacterial performance. Nanotechnology 29, 064001.
Shi, W., Guo, F., Chen, J., Che, G., Lin, X., 2014. Hydrothermal synthesis of $InVO_4$/Graphitic carbon nitride heterojunctions and excellent visible-light-driven photocatalytic performance for rhodamine B. Journal of Alloys and Compounds 612, 143-148.
Shi, Y., Hu, Y., Zhang, L., Yang, Z., Zhang, Q., Cui, H., Zhu, X., Wang, J., Chen, J., Wang, K., 2017. Palygorskite supported $BiVO_4$ photocatalyst for tetracycline hydrochloride removal. Applied Clay Science 137, 249-258.
Sivaranjanee, R., Saravanan, A., 2018. Carbon sphere: Synthesis, characterization and elimination of toxic Cr (VI) ions from aquatic system. Journal of Industrial and Engineering Chemistry 60, 307-320.
Sultana, M.-Y., Akratos, C.S., Pavlou, S., Vayenas, D.V., 2014. Chromium removal in constructed wetlands: a review. International Biodeterioration & Biodegradation 96, 181-190.
Sun, B., Zhou, W., Li, H., Ren, L., Qiao, P., Li, W., Fu, H., 2018. Synthesis of particulate hierarchical tandem heterojunctions toward optimized photocatalytic hydrogen production. Advanced materials 30, 1804282.
Wang, W., Yang, R., Li, T., Komarneni, S., Liu, B., 2021. Advances in recyclable and superior photocatalytic fibers: Material, construction, application and future perspective. Composites Part B: Engineering 205, 108512.
Wang, Y., Ding, K., Xu, R., Yu, D., Wang, W., Gao, P., Liu, B., 2020a. Fabrication of $BiVO_4$/$BiPO_4$/GO composite photocatalytic material for the visible light-driven degradation. Journal of Cleaner Production 247, 119108.
Wang, Y., Liu, M., Wu, C., Gao, J., Li, M., Xing, Z., Li, Z., Zhou, W., 2022. Hollow Nanoboxes Cu_2- xS@ $ZnIn_2S_4$ Core- Shell S- Scheme Heterojunction with Broad- Spectrum Response and Enhanced Photothermal- Photocatalytic Performance. Small 18, 2202544.
Wang, Y., Yu, D., Wang, W., Gao, P., Zhong, S., Zhang, L., Zhao, Q., Liu, B., 2020b. Synthesizing Co_3O_4-$BiVO_4$/g-C_3N_4 heterojunction composites for superior photocatalytic redox activity. Separation and Purification Technology 239, 116562.
Wu, S., Zheng, H., Lian, Y., Wu, Y., 2013. Preparation, characterization and enhanced visible-light photocatalytic activities of $BiPO_4$/$BiVO_4$ composites. Materials Research Bulletin 48, 2901-2907.
Xing, M., Qiu, B., Du, M., Zhu, Q., Wang, L., Zhang, J., 2017. Spatially separated CdS shells exposed with reduction surfaces for enhancing photocatalytic hydrogen evolution. Advanced Functional Materials 27, 1702624.
Yang, R., Dong, F., You, X., Liu, M., Zhong, S., Zhang, L., Liu, B., 2019. Facile synthesis and characterization of interface charge transfer heterojunction of Bi_2MoO_6 modified by Ag/AgCl photosensitive material with enhanced photocatalytic activity. Materials Letters 252, 272-276.
Yang, R., Zhong, S., Zhang, L., Liu, B., 2020a. PW_{12}/CN@ Bi_2WO_6 composite photocatalyst prepared based on organic-inorganic hybrid system for removing pollutants in water. Separation and Purification Technology 235, 116270.
Yang, R., Zhu, Z., Hu, C., Zhong, S., Zhang, L., Liu, B., Wang, W., 2020b. One-step preparation (3D/2D/2D) $BiVO_4$/$FeVO_4$@ rGO heterojunction composite photocatalyst for the removal of tetracycline and hexavalent chromium ions in water. Chemical Engineering Journal 390, 124522.
Zhang, H., Yu, D., Wang, W., Gao, P., Zhang, L., Zhong, S., Liu, B., 2019. Construction of a novel BON-Br-AgBr heterojunction photocatalysts as a direct Z-scheme system for efficient visible photocatalytic activity. Applied Surface Science 497, 143820.
Zhang, L., Wang, H., Chen, Z., Wong, P.K., Liu, J., 2011. Bi_2WO_6 micro/nano-structures: synthesis, modifications and visible-light-driven photocatalytic applications. Applied Catalysis B: Environmental 106, 1-13.
Zhao, W., Dong, Q., Sun, C., Xia, D., Huang, H., Yang, G., Wang, G., Leung, D.Y., 2021a. A novel Au/g-C_3N_4 nanosheets/CeO_2 hollow nanospheres plasmonic heterojunction photocatalysts for the photocatalytic reduction of hexavalent chromium and oxidation of oxytetracycline hydrochloride. Chemical Engineering Journal 409, 128185.
Zhao, W., Ma, S., Yang, G., Wang, G., Zhang, L., Xia, D., Huang, H., Cheng, Z., Xu, J., Sun, C., 2021b. Z-scheme Au decorated carbon nitride/cobalt tetroxide plasmonic heterojunction photocatalyst for catalytic reduction of hexavalent chromium and oxidation of Bisphenol A. Journal of hazardous materials 410, 124539.